

Elevated Hall Thruster Surface Sputtering due to Azimuthal Cathode Waves

IEPC-2022-381

*Presented at the 37th International Electric Propulsion Conference
Massachusetts Institute of Technology, Cambridge, MA, USA
June 19-23, 2022*

Parker J. Roberts ¹ and Benjamin A. Jorns ²
University of Michigan, Ann Arbor, Michigan, 48105

The influence of rotational cathode waves on the erosion of Hall thruster pole and cathode keeper surfaces is investigated experimentally. Laser-induced fluorescence measurements with temporal resolution up to 100 kHz are performed in the azimuthal direction in a high-power laboratory Hall thruster to discern the range of ion velocities near the exit plane of the device. Ions in the cathode plume are observed to swirl with speeds up to 2.5 km/s, and the azimuthal effective temperature of these ions ranges up to 9 eV. The ion density and mean azimuthal velocity are shown to oscillate strongly at a frequency of 90 kHz, corresponding to interactions with rotational anti-drift waves which propagate in the cathode plume. The spatial distribution of plasma wave amplitudes is demonstrated to correlate with metrics of ion energy, providing evidence of acceleration and heating of ions in the cathode plume. These ion energy data are then combined with empirical models for xenon sputtering to estimate the impact of the wave behavior on the erosion rates of pole cover surfaces. It is found that increased ion energies related to cathode wave interactions may account for the shape of the erosion rate profile near the inner edge of the inner pole, but additional mechanisms are required to account for the ion heating and erosion at the outer pole edge.

I. Nomenclature

IVDF	= Ion Velocity Distribution Function
MHMC MC	= Metropolis-Hastings Markov-Chain Monte Carlo
HERMeS	= Hall Effect Rocket with Magnetic Shielding
AEPS	= Advanced Electric Propulsion System
m_i	= ion mass
Z	= atomic number
e	= elementary charge
E_θ	= azimuthal electric field
$f_i(\vec{x}, \vec{v}, t)$	= ion velocity distribution function (s/m) ³
Y	= sputter yield (surface atoms per incident ion)
E	= incident energy of sputtering ions (eV)
α	= incident angle of sputtering ions (radians)
s_n	= Kr-C nuclear stopping potential
E_{th}	= Sputtering threshold energy
$Q, \lambda, \mu, w, \epsilon, \alpha_L$	= parameters of Eckstein model
β, γ	= parameters of Wei model
$\hat{\theta}$	= azimuthal direction

¹Ph.D. Candidate, Department of Aerospace Engineering, AIAA Student Member.

²Associate Professor, Department of Aerospace Engineering, AIAA Associate Fellow.

\hat{z}	= axial direction
ξ	= surface erosion rate (m/s)
R_{Keep}	= Radius of cathode keeper
ω	= angular frequency
I	= discharge current reference
$H(\omega)$	= transfer function

II. Introduction

The Hall thruster is a device for in-space propulsion which leverages an annular E×B configuration to produce thrust by expelling plasma at high speeds [1]. These devices avoid a limitation on thrust density due to space charge effects by maintaining a strong electric field in a quasineutral plasma rather than using biased grids [2]. While Hall thrusters are already widely used for near-Earth applications such as orbit raising and station keeping, their attractive performance metrics also make them prime candidates for cislunar and interplanetary electric propulsion mission architectures [3, 4]. A major challenge with developing Hall thrusters for these applications, however, is that mission timescales can require tens of thousands of hours of continuous operation [5]. Understanding and prolonging Hall thruster lifetime is therefore paramount.

To this end, “magnetic shielding” is a relatively new design iteration for Hall thrusters that has greatly extended their lifetime to > 10 kH. This stems from the fact that shielded thrusters adopt a magnetic field configuration that establishes a strong potential gradient directed away from the thruster walls. This reduces the erosion process that historically has dominated these systems, ion bombardment of the walls [6, 7]. With that said, while shielding has largely eliminated wall erosion, it has been found that these thrusters are subject to slower but still finite erosion on the front pole and cathode keeper surfaces [8]. Wear tests of these thrusters have shown gradual erosion of the front pole surface and cathode keeper at approximate rates of tens of $\mu\text{m/kh}$ [9, 10].

While this newfound pole erosion was determined to be sufficiently slow that it could be mitigated by employing thicker pole covers composed of low-sputter-yield materials [11], the mechanisms driving this erosion were not well understood. Follow-on studies attempted to elucidate this mechanism. For example, at high discharge voltages, Mikellides and Lopez Ortega showed that the erosion may be attributed to spatial shifts in the plasma potential structure correlated with the breathing mode oscillation [12]. However, the cause for the increased erosion rates measured at lower discharge voltages eluded prediction from simulations accounting for classical transport mechanisms alone [13]. In parallel, non-invasive experimental measurements of the time-averaged ion distribution near the inner pole in Hall thrusters revealed that the ions in this area had unusually high temperatures exceeding 10 eV [14, 15]. It was shown that these temperatures could lead to an order of magnitude increase in erosion in this area, and it has been suggested that at low discharge voltages, high ion temperatures may be a major driver for the anomalous pole erosion [12].

Despite evidence of these high temperature ions, however, it is not clear why they exist in this region. Indeed, fluid simulations based on classical transport theory underpredict the ion temperature in this region [12]. This discrepancy has led to detailed investigations of this so-called “anomalous” ion heating near the pole of Hall thrusters. One of the leading theories proposed to date is that the high-frequency lower-hybrid waves might grow unstable and heat ions in front of the pole surface [13, 16]. While this theory is plausible given the strong predicted growth rates for the lower hybrid waves in this region, these waves have not yet been observed experimentally in the pole region.

As an alternative theory, there are also large amplitude ($\sim 100\%$ variation in plasma potential compared to mean), coherent azimuthal plasma waves in this near pole region that have been experimentally documented. [17]. These rotational cathode waves, known as “anti-drift” modes due to their inverse scaling with the magnetic field strength, have been observed in a variety of Hall thrusters using high-speed imagery and Langmuir probes [15, 17–19]. In our previous work, we showed theoretically through a simplified quasilinear theory that these waves may be able to contribute directly to enhanced ion swirl and heating in this region [20]. More recently, we directly measured the acceleration of ions due to these waves in a standalone magnetized hollow cathode, demonstrating that these rotational waves have a strong influence on the ion population in the cathode plume [21]. However, the influence of these modes on the temperature of the ion population and their relevance to surface sputtering in a full Hall thruster discharge remains to be determined precisely. Thus, while these azimuthal modes appear to be a compelling candidate to explain the localized ion heating—and by extension erosion—this correlation has yet to be experimentally demonstrated.

To this end, this goal of this work is to investigate experimentally the extent to which these low-frequency, gradient-driven plasma waves influence erosion of the cathode keeper and pole surfaces in Hall thrusters with cylindrical symmetry and magnetic shielding. This paper is organized in the following way. In Section III, we provide an overview

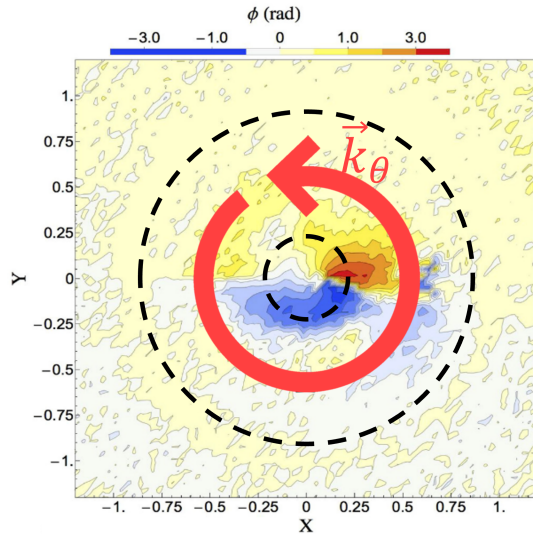


Fig. 1 Phase-correlated high-speed camera data from Ref. 17 demonstrating the azimuthal propagation of density waves near the central hollow cathode of a Hall thruster. Notional dashed lines represent the inner and outer radius of the inner pole.

of the interactions between anti-drift plasma waves and the ion species, as well as discuss a method for estimating erosion using empirical sputtering models. In Section IV, we then describe the experimental setup for laser-induced fluorescence measurements which we took in the H9 Hall thruster. This measurement technique allowed the non-invasive measurement of azimuthal ion velocities, from which plasma wave amplitudes and erosion estimates could be discerned. Sections V and VI contain the results of these investigations, followed by a discussion of the spatial correlations between wave amplitudes and ion energies, in addition to the calculation and analysis of erosion rates across the thruster face based on the observed ion behavior. Finally, Section VII summarizes the key results of this study.

III. Model for the Impact of Cathode Waves on Surface Erosion Properties

In this section, we briefly summarize the properties of the anti-drift plasma waves present in magnetized hollow cathode plumes. Following this, we provide a detailed description of the formulation used to estimate the contribution of azimuthal ion rotation in the cathode plume of a Hall thruster to the sputtering erosion rates for nearby graphite surfaces.

A. Overview of anti-drift rotational waves

Magnetized hollow cathode plumes give rise to steep gradients in the electric potential and plasma density, as charged particles expand rapidly from the cathode exit. In a Hall thruster with centrally mounted cathode, the cathode plasma environment can be modeled as a cylindrically symmetric geometry with a radial electric field and pressure gradient. This configuration leads to additive Hall and diamagnetic electron drifts in the azimuthal direction. These strong electron drifts in turn lead to the excitation of plasma instabilities. One such instability is a rotational wave known as an "anti-drift" mode. This plasma wave can be described by a multi-fluid formulation [17, 18, 21], and has been observed with high-speed imagery [17, 19, 22], plasma probes [18], and laser-induced fluorescence [21] in a variety of Hall thrusters and standalone magnetized cathodes. Figure 1 displays an example of high-speed camera data from a magnetically shielded Hall thruster in which each pixel is mapped to a phase delay relative to a reference pixel. This illustration notionally shows the primarily azimuthal direction of wave amplitude with a sketch of the approximate locations of the inner and outer radii of the inner pole surface.

While the mechanism for the growth of anti-drift waves in magnetized cathode plumes is the azimuthal electron drift, these waves can also interact with the ion species. This wave behavior manifests as simultaneous fluctuations in both the density n_1 and the electric field E_θ , primarily in the azimuthal direction. In the absence of collisions, the local

azimuthal ion velocity distribution $f_i(v_\theta, t) \propto n_i$ evolves according to the Vlasov equation

$$\frac{\partial f_i}{\partial t} + \vec{v} \cdot \nabla f_i + \frac{eE_\theta}{m_i} \frac{\partial f_i}{\partial v_\theta} = 0, \quad (1)$$

considering only the azimuthal component of the electric field. If the fluctuations in the field E_θ and the ion distribution f_i occur in-phase, the third term in Eq. 1 manifests as an effective force in the momentum equation, transferring net energy and momentum from the wave structures to the ion population when averaged over the wave period [21]. This results in a "spin-up" of the ion velocities in the azimuthal direction as ions expand axially and radially from the cathode exit. Azimuthal ion velocities and temperatures in excess of 2 km/s and 8 eV, respectively, have been observed in a standalone magnetized hollow cathode [21], but the mechanism (if any) for ion heating due to the presence of these waves is not yet well understood. In this study, we attempt to observe the impact of this mode on the ions in a full Hall thruster discharge in order to characterize the impact of these accelerated ions on the erosion characteristics of Hall thruster surfaces near the cathode plume.

B. Computation of Erosion Rate from Empirical Sputter Yield Models

In this subsection, we develop a framework for evaluating the degree to which azimuthal ion energies from cathode wave effects can influence the rate of erosion of the inner pole and cathode keeper. Erosion of plasma-facing surfaces occurs due to the sputtering of solid atoms by incident energetic ions [23]. For a single incident ion, the number of ejected sputterant particles is given on average by the sputter yield $Y(E, \alpha)$, which is a function of the incident ion kinetic energy E and impact angle α relative to surface normal. Various empirical and physics-based models exist for the sputter yield, where calibrated parameters adjust for details of the wall material and plasma species. These models typically treat the yield as a separable function $Y = Y(E, 0) \cdot Y'(\alpha)$, where $Y(E, 0)$ represents the sputter yield at normal incidence and $Y'(\alpha)$ contains the angular dependence.

We use the Eckstein model for normal-incidence sputtering [24, 25], which expresses the sputter yield as

$$Y(E, 0) = Qs_n \frac{\left(\frac{E}{E_{th}} - 1\right)^\mu}{\frac{\lambda}{w} + \left(\frac{E}{E_{th}} - 1\right)^\mu}. \quad (2)$$

The parameters Q , λ , E_{th} , and μ are free for fitting to experimental results, while w and s_n are given by empirical scaling relations based on the Kr-C nuclear stopping potential:

$$w = \epsilon + 0.1728\sqrt{\epsilon} + 0.008\epsilon^{0.1504}, \quad (3)$$

$$s_n = \frac{0.5 \ln(1 + 1.2288\epsilon)}{w}, \quad (4)$$

$$\epsilon = \frac{\alpha_L}{Z_{Xe}Z_C} \frac{4\pi\epsilon_0}{e^2} \frac{m_C}{m_{Xe} + m_C} E, \text{ and} \quad (5)$$

$$\alpha_L = \left(\frac{9\pi^2}{128}\right)^{1/3} \frac{a_B}{\sqrt{Z_{Xe}^{2/3} + Z_C^{2/3}}}, \quad (6)$$

where a_B is the Bohr radius and Z_j is the atomic number of element j . This model improves on previous physically-motivated models with empirical corrections, allowing good fitting near the low-energy sputtering threshold [24]. The Eckstein model also provides a larger number of tunable parameters compared to other analogous formulations, which allow for flexibility in fitting based on experimental data. We use fit parameters for the sputtering of carbon by singly-ionized xenon, corresponding to the graphite material commonly used for inner pole cover and cathode keeper surfaces in Hall thrusters [25].

We combine this normal-incidence model with the Wei function for angular dependence [26]. This relationship is expressed as

$$Y'(\alpha) = \frac{1}{\sqrt{1 + \beta^2 \tan^2 \alpha}} \exp \left[\frac{\gamma^2}{2} \left(\frac{1}{1 + \beta^2 \tan^2 \alpha} \right) \right], \quad (7)$$

where β and γ are free parameters. This angular model is chosen because recent mesh reflector sputtering experiments in a Hall thruster plume found the combined Eckstein-Wei model to provide the best fit with data when compared to

a variety of other models [27, 28]. We use the model parameters learned based on an assortment of experimental characterization tests by Yim et al using a Bayesian inference strategy [25].

To model the impact of azimuthal ion energies on the erosion rates of thruster surfaces, we assume that ions impacting the surface have negligible radial velocity, so that their sputter yield is solely determined by their swirl speed and axial velocity. We treat ions as monoenergetic in the axial direction, but account for time-dependent azimuthal velocity dispersion. This monoenergetic assumption is appropriate for our emphasis on azimuthal behavior because ions fall through a plasma sheath before reaching the surface, thereby gaining tens of eV of axial kinetic energy which dominate the flux to the surface. We note, however, that in a higher-fidelity treatment, the thermal spread in axial energies must be considered in order to accurately predict the precise erosion rates. In order to determine the axial energy with which ions impact thruster surfaces, we note that the thruster body is commonly maintained at cathode potential. The local plasma potential relative to the cathode fluctuates due to the wave behavior, so we represent the energy gained by ions as they fall through the sheath as

$$E_{axial} = e \langle \phi_p \rangle \left(1 + \frac{\tilde{\phi}_p}{\langle \phi_p \rangle} \right), \quad (8)$$

where $\langle \phi_p \rangle$ and $\tilde{\phi}_p$ are the steady and fluctuating plasma potential components.

The steady component of the plasma potential can be determined from time-averaged Langmuir probe data. In this work, we do not have access to direct time-resolved measurements of the plasma potential in the H9. However, the characteristics of fluctuations in plasma density can be observed with our laser-induced fluorescence experiment described in Sec. IV, in addition to the near-field ion saturation probe data taken in Ref. 18. The weak-amplitude theory of the cathode wave dispersion yields a linear relationship between the complex amplitudes of the potential $\tilde{\phi}_p$ and the density \tilde{n}_1/n_0 , given in Eq. 7 of that reference. We use this framework based on the background plasma property probe measurements in Ref. 18 to estimate the amplitude of the plasma potential fluctuations based on measurements of the density oscillations, and use these values to determine the time-resolved energy of ions impacting the pole and keeper surfaces in the axial direction.

A single ion with azimuthal speed v_θ impacts the surface with total kinetic energy

$$E = E_{axial} + \frac{1}{2} m_i v_\theta^2. \quad (9)$$

The impact angle is likewise given by

$$\alpha = \tan^{-1} \left(\frac{v_\theta}{v_z} \right), \quad (10)$$

where $v_z = \sqrt{2E_{axial}/m_i}$ is the axial velocity. At a given time t , the rotational ion velocities near the sputtering target are distributed according to a distribution function $f_i(v_\theta, t)$. We measure this function directly with the laser-induced fluorescence experiment described in Section IV. However, the measured IVDFs are not normalized, so we estimate approximate scaling by normalizing the measured distributions to unity, and multiplying by the average density measured in the H9 plasma in Ref. [18]. The time-averaged erosion rate ξ (in units of distance eroded per unit time) can then be calculated by integrating the scaled product of the sputter yield and incident ion flux over the velocity distribution and wave period, yielding

$$\xi = \frac{m_C}{\rho_C T} \int_0^T \int_{-\infty}^{\infty} v_z(t) Y(v_z(t), v_\theta) f_i(v_\theta, t) dv_\theta dt, \quad (11)$$

where T is the wave period, and m_C and ρ_C are the atomic mass and density of the carbon-graphite sputtering target. We performed this integration numerically, using double-Gaussian fits to the azimuthal distribution to reduce the effect of measurement noise.

IV. Experimental Characterization of Time-Resolved Ion Behavior

To address the possibility of ion energization induced by the rotating cathode mode, we performed a non-invasive laser experiment to measure the ion velocities in a high-power laboratory Hall thruster. The test article was the H9, a 9-kW class Hall thruster with a shielded magnetic field topography [29, 30]. This device shares design heritage with the 13-kW Hall Effect Rocket With Magnetic Shielding (HERMeS) developed for the Advanced Electric Propulsion

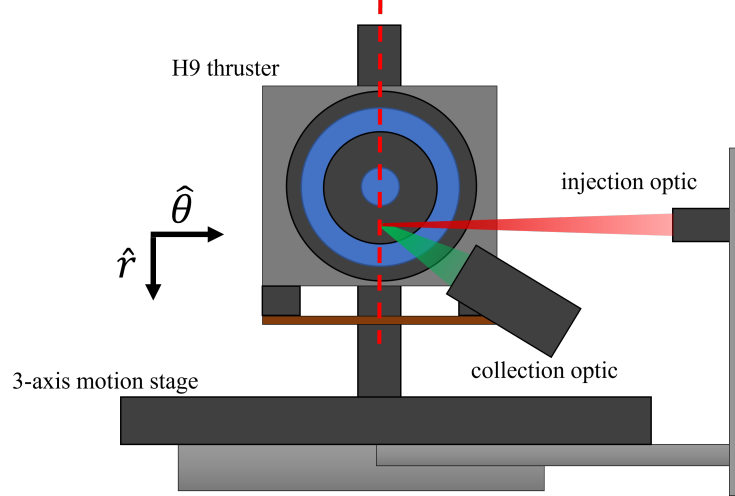


Fig. 2 Injection geometry for azimuthal laser-induced fluorescence. The shown curvilinear coordinate system is valid along the thruster center plane (red dashed line).

System (AEPS) on the Lunar Gateway and shares several features. These include a magnetically shielded topology, a center-mounted cathode (which provides a cylindrically symmetric configuration with an axial magnetic field applied to the cathode plume), and graphite pole covers.

In this experiment, we maintained the H9 at its nominal discharge voltage and current of 300 V and 15 A, respectively, yielding an average power of 4.5 kW. We electrically tied the body of the thruster to the cathode. We tested the H9 in the Large Vacuum Test Facility (LVTF), a vacuum chamber which is 6 meters in diameter and 9 meters in length [31]. An array of cryopumps held the chamber xenon pressure at 5 μ torr during thruster operation.

We measured the distribution of ion velocities with laser-induced fluorescence of the electronic transition from the metastable state $5p^4(^3P_2)5d^2[4]_{7/2}$ to the state $5p^4(^3P_2)6p^2[3]_{5/2}^o$ in singly-ionized xenon (Xe II) [32]. This transition is pumped by photons at a wavelength at $\lambda_0 = 834.953$ nm in vacuum, and decays to a lower state by emitting light with a wavelength of 541.2 nm. With the use of a tunable diode laser, we focused coherent light at a range of wavelengths near λ_0 to a 1-mm spot in the plasma. We collected fluorescent photons from a small volume surrounding the focal point to obtain a Doppler-broadened lineshape for the transition, which reflects the distribution of velocities of ions in the targeted metastable state according to the Doppler shift

$$v = c (1 - \lambda/\lambda_0), \quad (12)$$

where v represents the ion velocity component along the laser wavevector, c is the speed of light, and λ/λ_0 is the fractional shift of the lab-frame wavelength due to laser detuning. The convention we use in this case defines positive velocities as pointing against the laser photon wavevector.

Optical fibers coupled the injected laser light to a 50-mm-diameter focusing optic within the chamber. This optic emitted photons with a direction such that the wavevector passed transversely across the face of the thruster. When aligned to the 6 o'clock vertical diameter of the cylindrical thruster face, the Doppler relation picks out the azimuthal component of the ion velocities. This geometric configuration is displayed in Fig. 2. A 75-mm-diameter lens imaged the collected fluorescence into a 1-mm optical fiber, which coupled this light into a photomultiplier tube (PMT) detector. A passive notch filter rejected stray light by attenuating wavelengths outside this range.

Even after line filtering, intense background light from the plasma buries the LIF signal in noise. To alleviate this, we used a phase-sensitive detection (PSD) scheme to extract the intensity of light at the fluorescence wavelength corresponding to the laser excitation response. For time-averaged ion velocity measurements, we implemented a Stanford Research Systems SRS-830 lock-in amplifier. A mechanical chopper modulated the injected intensity at a frequency of 2 kHz. Phase-sensitive detection with a lock-in time constant of $\tau_{PSD} = 1$ s was sufficient to obtain high signal-to-noise ratio (SNR) for the azimuthal velocity distributions, but effectively averages out effects on the time scale of faster plasma oscillations such as the rotating cathode mode.

LIF measurements with enhanced time-resolution are possible through the use of faster beam modulation and additional signal processing. For up to 100-kHz resolution, a solid-state acousto-optic modulator (AOM) chopped the

laser at a higher frequency of 1.5 MHz. A 10-k Ω resistor shunted the PMT current for a fast response. An Alazartech ATS9462 digitizer card recorded this signal at a sample rate of 30 MS/s for long acquisition periods of 30 s per wavelength. The digitizer streamed directly to a fast PCIE-coupled SSD, with the full dataset taking up nearly 2 TB of drive storage.

In this work, we use the transfer function averaging technique developed by Durot to achieve time-resolved LIF [33]. We divided each 30-s acquisition into thousands of time segments for analysis. Two stages of signal processing then denoised the LIF signal from this segmented dataset. First, a post-processing script performs phase-sensitive detection on each segment. We used a fast time constant of $\tau_{PSD} = 700$ ns. This time constant sets the effective bandwidth limit, leading to more than 10% attenuation of frequency components above 100 kHz [34]. This PSD step improves the signal strength relative to the noise by a reasonable amount, but still is not sufficient for true time-resolution, since the shorter time constant is not able to average out enough noise. To overcome this, we next computed average linear transfer functions in the frequency domain $H(\omega)$ by comparing the FFT of each signal trace $f(\omega)$ to the FFT of a reference signal $I(\omega)$ with higher SNR, satisfying the relationship

$$f(\omega) = H(\omega) \cdot I(\omega). \quad (13)$$

In this case, we used the discharge current, which was simultaneously streamed with the digitizer card, as the reference signal. Averaging these transfer functions over all segments provides a denoised relationship which enables the reconstruction of synchronous LIF time-traces at each position and wavelength from a single reference trace. Time-resolved IVDFs are then reconstructed from a reference trace by inverting the relationship in Eq. 13.

We processed both the time-averaged and time-resolved data in a similar fashion. Curve fits to sums of two Gaussian distributions approximated the data analytically while accounting for nonequilibrium features, and analytical relationships based on the fit parameters produced moments of these distributions including the mean velocity and ion temperature (defined kinetically as the variance in ion kinetic energy). A Bayesian framework with Metropolis-Hastings Markov-Chain Monte Carlo (MHMCMC) sampling quantified the statistical error in these reduced data based on the fitting uncertainty. This IVDF analysis framework is described in detail in Ref. 21. Time-resolved IVDFs were downsampled to a lower frame rate to reduce the dataset size while still capturing resolvable features before fitting. This allowed comparison of the time-averaged velocity and temperature of the ion fluid with "instantaneous" moments of the time-resolved distribution. Note that since the oscillating IVDF is not in equilibrium, a fluid approximation is not necessarily valid and care is required in discussing the meaning of the ion temperature measured via this method. As demonstrated in Eq. 11, for the purpose of measuring erosion, the most important quantity is the integrated flux of energetic ions, which more is more directly tied to erosion properties than the bulk fluid moments.

V. Results

A. Time-Averaged Ion Motion

In this section, we present the results of the azimuthal LIF experiment described in Section IV. Figure 3a displays phase space contours of the time-averaged azimuthal ion velocities across the radial span of the H9, at an axial distance of 5 mm downstream from the thruster exit plane. We superimpose the mean velocity in each measurement location. Figure 3b shows the radial variation of azimuthal ion temperature, which characterizes the spread in ion kinetic energy along that direction. All radial positions are normalized to the radius of the cathode keeper, denoted R_{keeper} . Uncertainties for the fluid moments are computed via MHMCMC sampling of fits based on the multi-Gaussian noise model described in Section IV. The 1- σ error bars are smaller than the marker size for the mean velocities in Fig. 3a.

Fig. 3 displays three distinct regions of behavior of azimuthal time-averaged velocities. Up to the outer radius of the keeper (1 on the horizontal axis), a strong ion swirl drift is observed which grows linearly with distance from the center axis, up to 2.5 km/s. The contour plot demonstrates that in addition to this net swirl, there are a significant number of ions in the tail of the distribution with velocities exceeding 5 km/s, which corresponds to 15 eV of kinetic energy. We plot data from both sides of the thruster centerline (red dashed line in Fig. 2) in the cathode keeper region to demonstrate the cylindrical symmetry of the ion drift across the keeper face, where negative velocities on the left side demonstrate global rotation of the ion species centered on the cathode center axis. The temperature of these cathode ions also enhances with radial distance along with the velocity, reaching a peak of nearly 9 eV in front of the keeper face.

Between 1 and about 5 keeper radii, we measure ions swirling in front of the inner pole of the thruster. These ions still exhibit a relatively large mean swirl velocity of about 1.5 km/s which is nearly constant across the pole cover. This mean velocity is reduced by about a factor of 2 compared to the keeper edge, however. In this case, there is a large

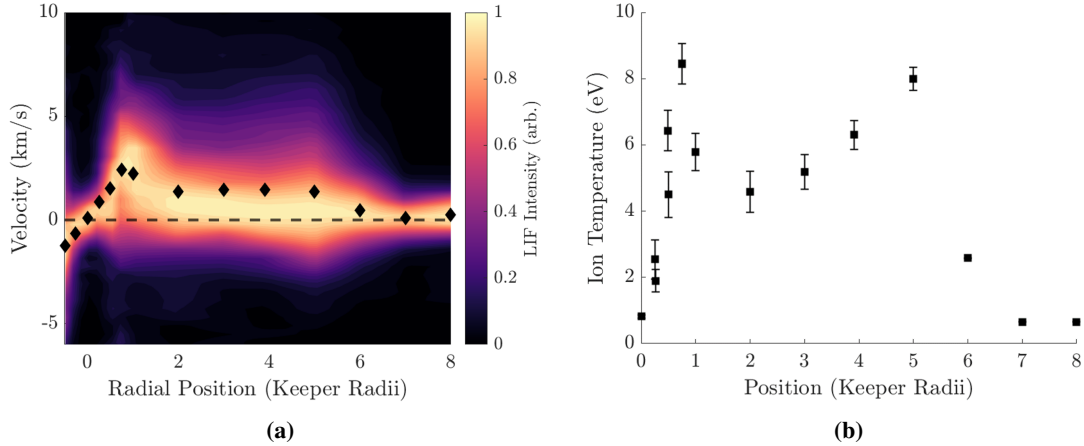


Fig. 3 a) Spatial variation of the time-averaged azimuthal, normalized ion velocity distribution with radial position at a downstream location of 5 mm. Mean velocities are denoted with black markers. b) Kinetic ion temperature plotted against radial position.

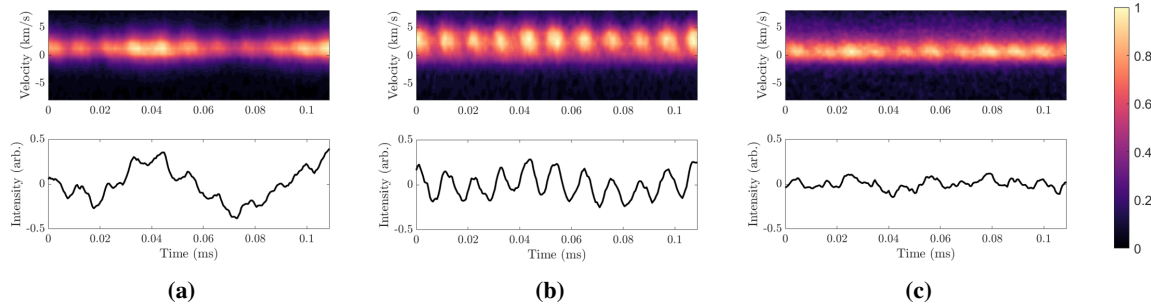


Fig. 4 Time-resolved azimuthal velocity distributions with plots of the normalized fluctuation n_1/n_0 based on the total LIF signal intensity. a) mid-keeper, b) keeper edge, c) mid-inner-pole. The IVDF intensity colorbar, in arbitrary units, is normalized to the maximum of the time-resolved distribution at each location.

discrepancy between the mean velocity and the most probable velocity. This is characteristic of a high-energy "tail" to the distribution. Ions near the outer edge of the inner pole (~ 5 keeper radii) exhibit large temperatures as well, climbing back up to 8 eV near the outer edge.

Finally, the azimuthal speed of ions exiting the channel (≥ 6 keeper radii) is less than that of the pole and cathode ions. These distributions are relatively cold, with the mean velocity and most probable velocity overlapping in Fig. 3a. The azimuthal ion temperatures in this region also fall below 1 eV, with low fitting uncertainty due to the highly Maxwellian nature of the distributions (see Fig. 6). Mechanisms for the strongly nonlinear dependence of ion velocity and temperature on radius from the thruster axis suggests interactions between competing local plasma phenomena which heat and accelerate the ions in different ways, as discussed further in Section VI.

B. Time-Resolved Ion Motion

In order to characterize the impact of low-frequency cathode wave structures on the ion velocity distribution, we performed time-resolved LIF measurements using the transfer function estimation approach described in Sec. IV. Figure 4 shows the time-resolved ion velocity distributions measured with this technique. We measured the fluctuations of the ion population below 100 kHz in 3 locations: midway across the keeper radius ($0.5 \cdot R_{Keeper}$, Fig. 4a), at the outer edge of the keeper ($1 \cdot R_{Keeper}$, Fig. 4b), and midway across the inner pole ($3 \cdot R_{Keeper}$, Fig. 4c).

The total intensity of the time-resolved LIF signal oscillates strongly in time. We plot this in the lower panels of Fig.

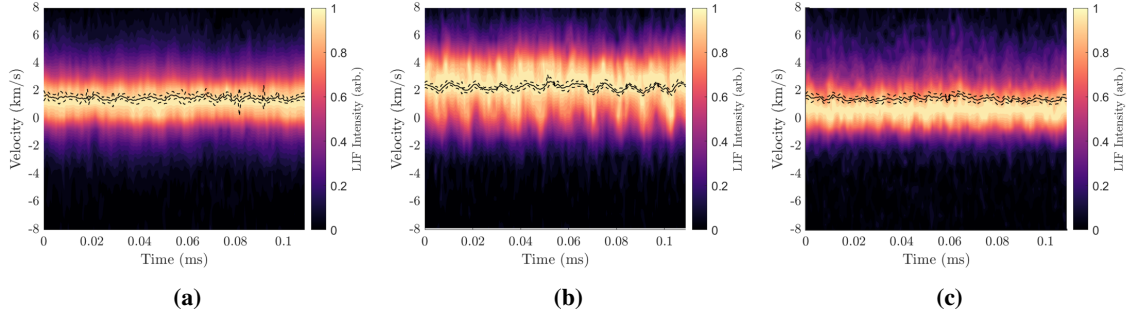


Fig. 5 Time-resolved azimuthal ion velocity distribution functions at the mid-keeper (a), keeper edge (b), and mid-pole (c) radial locations. At each time step, the distribution is normalized to its maximum, and the mean velocity is shown with $1\text{-}\sigma$ uncertainty bounds.

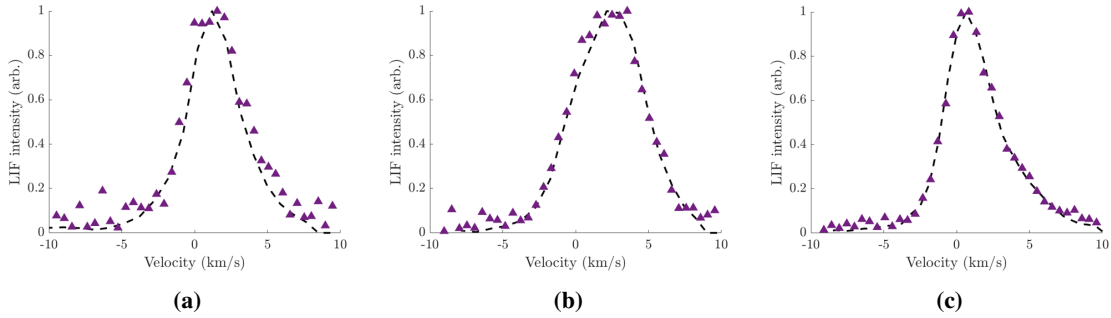


Fig. 6 Comparison between time-averaged and time-resolved azimuthal ion velocity distributions at the mid-keeper (a), keeper edge (b), and pole (c). The triangles correspond to time-averaged LIF data taken with a hardware lock-in amplifier, while the dashed lines correspond to the time-average of the time-resolved distribution.

4 by integrating the measured distribution numerically over velocity. Subject to the assumption that the metastable state targeted by this LIF configuration is representative of the overall ion population, this measure of the total intensity serves as a scaled proxy for the total ion density $n_i(t)$. In the keeper region, Fig. 4a demonstrates two superposed oscillatory phenomena at disparate frequencies. First, a 10-20 kHz oscillation in the intensity of the distribution is observed. This fluctuation matches the frequency of the thruster breathing mode, a low-frequency global current oscillation ubiquitous in Hall thrusters. Second, we find faster, $\sim 90\text{-kHz}$ variations in the total fluorescent light, which corresponds to the frequency of the fundamental anti-drift mode previously observed in the H9 thruster with Langmuir probes [18].

The keeper edge region (Fig. 4b) demonstrates a similar fluctuation in the total intensity, but in this location, coherent, 90-kHz oscillations occur with much larger amplitude than the relatively-subtle breathing-mode structure. This is likely due to the fact that the cathode wave amplitude is known to peak off-centerline [18], while the lower-frequency global discharge current oscillations are expected to fall off with radial distance from the cathode, since the electron current is primarily directed along axial field lines at the cathode exit. The mid-pole-region ion distribution shown in Fig. 4c exhibits some frequency content at the 90-kHz cathode wave frequency, but the intensity fluctuations are largely turbulent and much weaker here. A significant high-energy tail to this distribution is present throughout these oscillations, and in fact the contour plot demonstrates that this high-energy tail is relatively constant in height, while the primary population of beam ions weakly oscillates in intensity in-phase with the stronger oscillations at reduced radii.

In Fig. 5, we normalize the time-resolved ion distributions to their respective maxima at each time step in order to reveal variations in the relative proportions of ions moving at different azimuthal speeds. The keeper and keeper edge distributions, shown in Figs. 5a and 5b, respectively, demonstrate moderate acceleration and deceleration of the ion fluid at the 90-kHz wave frequency. Notably, the strong intensity oscillations at the lower, breathing-mode frequency do not contribute meaningfully to acceleration of the ion population on that time scale in Fig. 5a. The distribution at the keeper edge displays the largest and most coherent fluctuations in mean velocity, with a peak-to-peak amplitude of $\lesssim 1$ km/s.

Fig. 6 compares the time-average of the time-resolved LIF data (dashed lines) with the true time-averaged LIF data

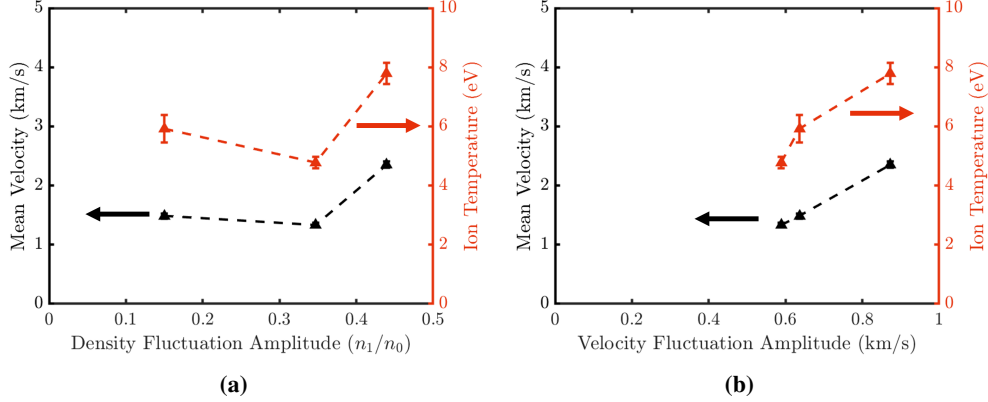


Fig. 7 Ion velocity and temperature plotted over the amplitude of fluctuations in a) ion density and b) ion velocity.

acquired with a hardware lock-in amplifier. These distributions are normalized such that each is maximized at unity. The time-averaged distributions agree well with the time-resolved technique. The azimuthal IVDF at the mid-keeper position is Maxwellian with a small net drift of < 1 km/s. The keeper edge distribution demonstrates broadening and increased drift, commensurate with the large mean velocity and temperature shown in Fig. 3. Finally, the time-averaged pole distribution is composed of a primary population with a smaller drift. The mean drift speed, however, is inflated by the high-energy tail. As noted above, there is measurable ion content in this tail at rotational velocities up to 10 km/s.

VI. Discussion

In this section, we first present and discuss the spatial correlations between the low-frequency ion fluctuations and the presence of energetic ions. Next, we compute estimated erosion rates for a variety of assumptions in order to demonstrate the effect of azimuthal ion swirl on predicting Hall thruster erosion.

A. Correlation between wave amplitude and ion energy

The results of the time-resolved LIF experiment demonstrate that in the near field, the plasma in front of the outer edge of the cathode keeper displays large fluctuations in both the ion density as well as the ion velocities. These fluctuations occur at the same frequency (90 kHz) as the anti-drift mode previously measured in the H9 cathode via high-speed probing methods. This directly shows that the primarily azimuthal electric field oscillations which make up the wave are able to push and pull on the ions in that direction during each wave period, accelerating and decelerating the bulk population. This motion is consistent with the theory of weak-amplitude electrostatic plasma waves at this low frequency relative to the plasma frequency ($\omega \ll \omega_{pe}$), in which waves are subject to the assumption of quasineutrality, meaning that ion oscillations respond to oscillations in the electron fluid to prevent local charge buildup.

The same position in the plasma where ion oscillation amplitudes are maximized also corresponds to elevated time-averaged metrics of ion energy in the azimuthal direction, including both the mean azimuthal velocity as well as the kinetic ion temperature. This spatial correlation implies that the ion drift speed and breadth of energies is related to the amplitude of the cathode anti-drift mode. Figure 7 visualizes this correlation by showing the variation of the ion velocity and temperature against two measurements of the cathode wave amplitude: the amplitude of ion density (LIF intensity) fluctuations in Fig. 7a, and the amplitude of mean velocity fluctuations in Fig. 7b. For the two locations with the largest density fluctuation (both near the cathode), a strong increase in both the temperature and velocity of the ions in the azimuthal direction is observable. However, the velocities and temperatures are still large in the pole, despite a lower amplitude of density fluctuations, making the overall trend with density amplitude nonlinear. This fits our general observation that ion energies are strongly tied to the presence and amplitude of rotational waves near the cathode, but additional heating mechanisms may be present farther out radially into the pole region.

In general, the correlation between ion energies and density wave amplitudes is reduced at the outer edge of the pole compared to the cathode measurement positions. As expected, the time-resolved measurements reveal that the ion density amplitude at the wave frequency decays with radial distance, and coherent oscillations give way to chaotic

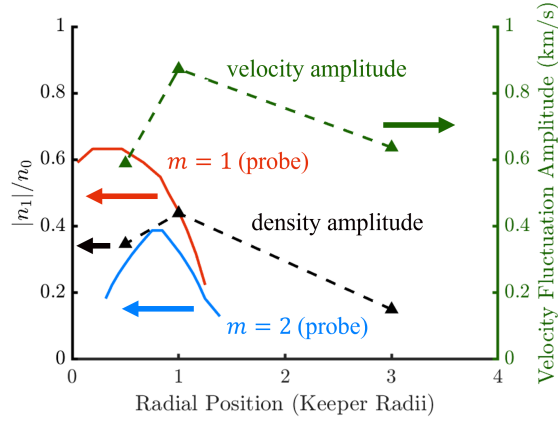


Fig. 8 a) Comparison of wave amplitude inferred from downstream probe measurements[18], ion density fluctuations, and ion velocity fluctuations. Probe measurements were performed 2 keeper radii downstream of LIF measurements.

fluctuations at large keeper radii. This lessened low-frequency wave activity at the outer edge of the inner pole region corresponds with reduced drift velocities, however the mean ion swirl reaches a nearly constant value of 1.5 km/s in front of the pole rather than reducing further. While the ion temperatures cool to 5 eV at increasing radii from the inner pole edge location of maximum wave amplitude, a second hot-spot is observed at the outer edge of the pole despite the lack of low-frequency wave activity here. These two distinct regions of heated ions are likely due to separate plasma phenomena. We note that these increased ion temperatures near the outer edge of the inner pole are consistent with the calculated growth rates of the higher-frequency modified two-stream instability from Lopez Ortega et al., for example in Fig. 6 of Ref. 12. These higher-frequency waves have proposed as a heating mechanism for ions which impact the pole, and the total radial distribution of ion energies may depend on the total contribution of these plasma wave phenomena at disparate frequencies.

A more uniform correlation with fluid moments is present when the wave amplitude is represented in terms of the mean velocity fluctuations (Fig. 7b). This is due to the fact that the mean velocity of the outer pole population oscillates with a larger amplitude than the total intensity of the distribution in that location. Upon inspecting Fig. 4c, this discrepancy appears to be caused by the relative heights of the primary/cold ion population and the accelerated ions in the high energy tail varying in phase with the cathode wave frequency. The tail of the distribution appears to be relatively unaffected by the low-frequency waves, while the slower ions do oscillate in intensity along with the ions in other locations. This suggests that the cathode wave behavior still exerts influence over the ion distribution at larger radii, but it is likely that a separate mechanism is responsible for the production of the high-energy tail in particular, perhaps at a higher frequency than the 100-kHz bandwidth limitation of this LIF diagnostic. Indeed, this flattening of the distribution at high speeds is consistent with the qualitative characteristics of nonlinear interactions between ions and kinetic instabilities in general, and it is possible that this distribution is tied to the presence of higher-frequency waves which are able to effectively "heat" the ions by increasing the spread in thermal energy along multiple directions.

Figure 8 shows measurements of the first two modes of the 90-kHz ion density fluctuation amplitudes, as recorded by high-speed ion saturation probes in a previous experiment with the H9 [18]. Due to their limited lifetime and tendency to perturb the discharge, these probes were injected on a fast axial translation stage to a distance of 2 cm downstream, a factor of 4 farther from the thruster exit plane than possible with the non-invasive LIF diagnostic. The qualitative characteristics of the probe measurements agree with the LIF technique. Both of these diagnostics measure wave amplitudes which are maximized off-centerline in a localized region. The exact position of this region differs between the two measurements, however, with the maximum LIF wave amplitude occurring at the outer edge of the keeper rather than in front of the keeper face. We note that the LIF amplitude measurements lack sufficient spatial resolution to localize the peak of the amplitudes entirely, but based on the correlation demonstrated above, we can infer from the maximum mean velocity and temperatures that the wave amplitudes are likely largest near 0.75 keeper radii, as compared to the 0.5 keeper radii value from the $m = 1$ probe data.

The reason for this discrepancy is unknown, but it is likely that the growth conditions for the wave vary with axial position due to nonuniformities in the magnetic field, electric potential, and density as the plasma rapidly expands

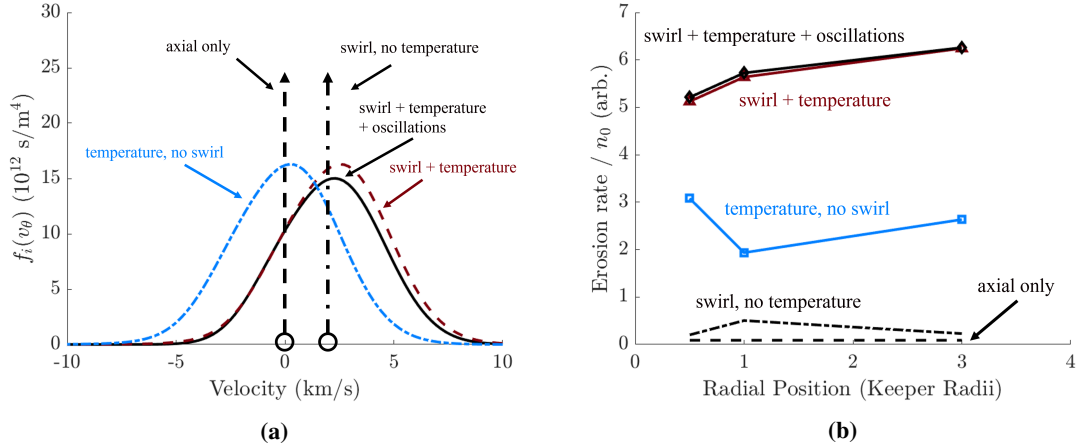


Fig. 9 a) Sample ion VDFs used for calculations of the surface erosion rate. b) Radial distribution of density-normalized erosion rates estimated with various azimuthal ion VDFs.

outward from the cathode, leading to small differences in wave characteristics over the 1.5-cm axial distance traversed by the plasma between the LIF and probe measurement location. Another possibility is that the impact of the waves on the ion population is tied to the expansion of the ions radially from the cathode exit due to the strong pressure gradient there, leading to a convective delay in the measurable effect of plasma oscillations until the ion fluid has expanded to larger radii. Regardless, the characteristics of the ion distribution near the cathode plume demonstrate strong coupling between low-frequency wave behavior and ion energization. We therefore propose that the high velocities and temperatures at the keeper outer edge are due to the large low-frequency perturbations to the ion fluid found there. We have previously shown using the theory of weak plasma turbulence that these waves can directly act back on the ion population to accelerate the bulk velocity up to 2-3 km/s on the time scale of ion expansion from the cathode [21]. However, the mechanism (if any) for ion heating via this low-frequency mode remains elusive, and may be caused by interactions with higher-frequency waves above the LIF detection limit or stronger nonlinear interactions with the ion distribution. While this ion heating must still be investigated to provide a complete causal framework for understanding the observed energies, a clear mechanism and experimental correlation is observable for which these waves can transfer significant energy to cathode ions through the azimuthal swirl drift.

B. Estimation of wave-induced erosion rates

We applied the erosion estimation framework described in Section III.B to the measured ion velocity distributions to analyze the impact of the observed azimuthal energies on the erosion rates near the poles. In order to isolate the contribution of various characteristics of the distribution to the erosion rates, we performed these calculations with 5 test cases for the azimuthal ion distribution. For all cases, we ignored radial motion of the ion population, and only considered a Dirac distribution in the axial direction corresponding to monoenergetic axial ions. We then attribute the axial impact velocity to that acquired by a stationary ion after falling through the plasma sheath, informed by probe measurements of the background plasma potential ($\sim 24 \text{ V}$) and conservation of energy. We note that due to these assumptions, the numerical values of the calculated erosion speeds are not necessarily representative of precise wear estimates. However, these calculations are illustrative to the effect of azimuthal ion thermalization and swirl on the erosion characteristics of Hall thruster surfaces such as the inner pole and cathode keeper.

Figure 9 displays the velocity test cases (a) and the resulting erosion rates (b). We note that in accordance with Eq. 11, the actual erosion rate is strongly dependent on the local plasma density, since the total flux of ions scales directly with n_i regardless of energy. The Langmuir probe measurements invoked to carry out these calculations display a rapid drop-off in the density with radius, which dominates the radial trend in erosion. In order to more clearly illustrate the dependence of the shape and characteristics of the IVDF on influencing the erosion rate, we therefore plot the estimated erosion rate normalized to the local plasma density in Fig. 9b.

The first velocity distribution tested is the baseline, with a monoenergetic axial population based on the sheath potential energy and zero azimuthal swirl velocity, shown as a dashed line. Secondly, we consider a monoenergetic ion

population with the mean velocity of the measured time-averaged IVDF in the azimuthal direction (dash-dot line). This monoenergetic erosion is increased when accounting for the swirl energy, but in both cases these ion distributions cause below 1 $\mu\text{m}/\text{kh}$ of erosion, which is much smaller than the rates achieved by the thermal populations. We next consider the time-averaged IVDF, but shift the mean velocity such that the bulk ion population has the measured temperature but zero net swirl. This distribution, shown in blue, leads to 3-10 \times the erosion caused by the monoenergetic populations, with the greatest increase found in the cathode keeper position nearest centerline. The fact that including the breadth of the distribution has the largest effect in the location with the coldest ion temperature (Fig. 3b) is curious, but can be explained by examining the qualitative characteristics of the distribution function (Fig. 6a). Despite having a reduced effective temperature due to the relatively narrow central peak of the distribution, the VDF in this position has small but measurable ion content in the far tails of the distribution from -5 to 8 km/s of azimuthal velocity. When combined with the strongly nonlinear increase of sputter yield with both ion energy and angle of incidence, these few energetic ions contribute disproportionately to the total erosion rate.

We next consider the erosion due to both the bulk azimuthal swirl and full shape of the time-averaged VDF, shown in maroon. Including the strong azimuthal ion drift leads to an increase in the erosion rates by a factor of 1.5 to 3 in the cathode region when compared to the stationary thermal population. While the monoenergetic drifting ions did not lead to significant erosion, the combination of bulk swirl with thermal ions has a large effect. This is due again to the strong sensitivity of erosion rates to relatively small numbers of energetic ions in the tails of the distribution; accounting for the actual drift of the ions pushes the thermal tail of the distribution to even higher energies, which dramatically increases the erosion rates. This increase is most dramatic in the region at the keeper edge where both wave amplitudes and ion swirl speeds were measured to be large. The relative contribution of the swirl speed is reduced in front of the keeper, where the azimuthal drift is lesser. Lastly, we consider the full measured time-resolved ion distributions to account for ion flux variations on the wave time scale. For this case, we account for oscillations in the accelerating potential of the sheath by imposing potential fluctuations on the plasma potential relative to the thruster body. These fluctuations are derived according to the linear dispersion relation of the anti-drift mode along with the background plasma properties measured in the aforementioned Langmuir probe experiment presented in Ref 18. The phase shift between the directly-measured LIF intensity fluctuations and the potential is found to be negligible due to the relatively low electron collisionality assumed in this region, below 10^6 s^{-1} [18]. Only minute differences are present between the full time-averaged VDF erosion rates and the mean time-resolved erosion rates. Differences in these two estimations can be traced to the product of the time-dependent components of the integrand in Eq. 11. The small nature of these deviations suggests that the contribution of the oscillations manifests primarily through the oscillating velocity distribution $f(v_\theta, t)$, with only small changes due to the potential oscillations.

The erosion rate estimates based on the time-resolved data suggest that the contribution to erosion over the period of the oscillations is well-represented by the time-averaged IVDF. Armed with this insight, we plot the erosion rates predicted by the time-averaged LIF data with increased spatial resolution in Fig. 10. Figure 10a demonstrates the erosion rate across the normalized keeper radius, while Fig. 10b displays the erosion across the normalized inner pole radius, where zero corresponds to the inner radius of the inner pole. We also include for comparison on these plots the measured erosion rates from wear tests of the HERMeS, reported in Ref. 10. While the H9 and HERMeS are thrusters of different sizes, they share many characteristics, and this data may provide qualitative insight into general trends in the erosion characteristics near the cathode plume. For the reported data, the HERMeS was operated at the same discharge voltage as the H9 (300 V), but at a higher discharge current of 20.8 A [10]. The keeper erosion rate data was also reported with a 25%-higher magnetic field strength than the nominal setting. In presenting this comparison, we also note that due to the difference in thruster and the neglect of the axial ion temperature and radial ion velocities, these erosion estimates are not meant to be interpreted as predictive values, but rather as general trends which highlight the contribution of wave-driven azimuthal ion drift to surface erosion. Additionally, this diagnostic and our analysis do not account for multiply-charged species, which if present in any significant quantity would experience increased acceleration by the wave electric field structures and increase the flux of energetic ions to these surfaces.

Figure 10a demonstrates a complex trend in the keeper erosion rates, which is not necessarily consistent between the estimated erosion and measured sputtering rates. This behavior is likely highly dependent on the material properties and axial ion distribution for ions exiting the cathode. However, the approximate magnitude of the erosion does agree roughly with our calculations. The measured pole erosion rate (Fig. 10b) demonstrates a dip in the center of the pole, with elevated erosion rates at the edges close to the denser cathode and channel regions of the plasma. The calculated erosion rate is generally lower than the measured rate by more than an order of magnitude, likely due to the assumption of monoenergetic axial ions. If the distributions with large ion temperatures measured azimuthally are even remotely isotropic, the correspondingly large spread in axial energy will lead to increased erosion across the entire pole,

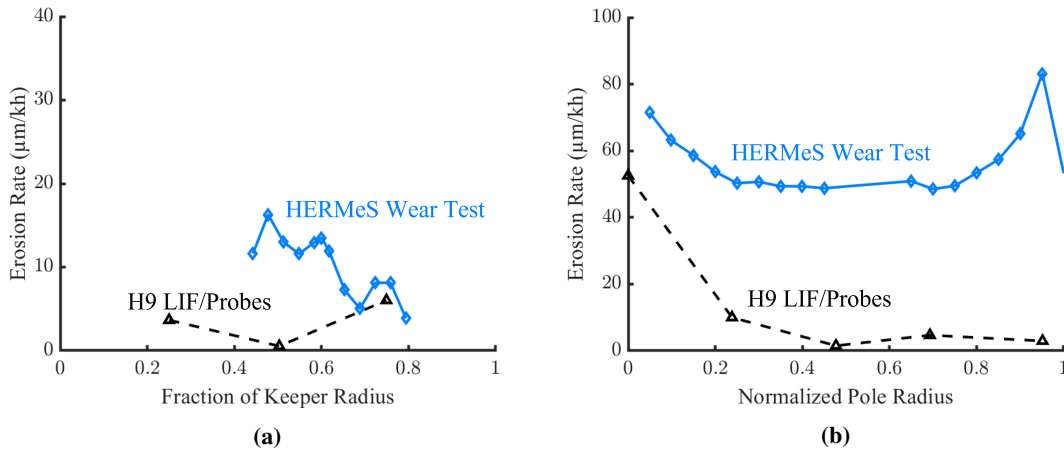


Fig. 10 Comparison between estimated erosion rates in the H9 and measured erosion rates in the HERMeS [10] across the keeper face (a) and inner pole (b).

where temperatures are large according to the time-averaged LIF measurements. Notably, however, our calculations do reproduce a key aspect of the measured erosion profile, which is the sharp decay from a local maximum at the inner radius of the pole. This position corresponds to the largest amplitude of measured cathode waves, in addition to the largest time-averaged swirl speeds and azimuthal temperatures measured in the H9. This therefore suggests that the total erosion characteristics of the front pole and keeper surface in magnetically shielded Hall thrusters with central cathodes are complex and strongly dependent on the 3D characteristics of the local ion distribution. With that said, there is a strong link between the presence of rotating cathode waves, fast azimuthal ion drift/heating, and elevated erosion at the inner edge of the front pole surface. This necessitates considering both these low-frequency phenomena in addition to higher-frequency heating mechanisms for a first-principles analysis of the erosion of thruster components.

VII. Conclusion

We performed time-resolved laser-induced fluorescence measurements in a high-power, magnetically shielded Hall thruster to investigate the impact of azimuthal cathode waves on the sputtering rate of nearby surfaces. These measurements demonstrate strong fluctuations in both the density and azimuthal velocity of ions at the 90-kHz frequency of the anti-drift rotational cathode mode. We observed varied kinetic properties of the ion fluid across the radial profile of the Hall thruster, with 90-kHz oscillations confined to the keeper/inner pole region, and lower-amplitude, turbulent fluctuations present at the outer edge of the pole. Non-equilibrium IVDFs are present in the outer edge of the pole region, which may be related to wave phenomena occurring at a higher frequency than the 100-kHz detection limit of the particular diagnostic implemented in this study.

Time-averaged LIF measurements show distinct regions of azimuthal ion velocities and kinetic temperatures in the Hall thruster near-field. A hot-spot with fast-drifting ions up to 3 km/s and azimuthal temperatures up to 9 eV corresponds to the location of maximum cathode wave amplitude, at the outer edge of the cathode keeper. However, a separate region of hot ions (~ 8 eV) is observed near the outer edge of the inner pole, where the cathode wave behavior is lessened. This suggests that multiple plasma wave phenomena may be tied to the ion heating and acceleration which lead to elevated erosion of the inner and outer edges of the inner pole in Hall thrusters. The time-resolved data and spatial correlation with time-averaged energy metrics demonstrates a strong coupling between rotational cathode modes and the ion distribution, and previous work has demonstrated a theoretical mechanism for time-averaged acceleration consistent with these measurements. However, more work is required to establish a concrete theoretical basis for the link, if any, between the large temperatures observed near the cathode keeper and the wave behavior present there.

We invoked empirical sputter yield models and Langmuir probe measurements of the background plasma properties to estimate erosion rates at the front pole for a variety of data-driven assumptions about the distribution of ion energies. This allowed for the isolation of the contribution of the thermal spread of the ions vs. the net ion drift in the azimuthal direction to erosion rates. These erosion calculations demonstrate that the combination of net drift and elevated temperature are necessary to fully account for erosion rates, and considering just one of these metrics leads to large

underpredictions for erosion rates. This result suggests that a full characterization of Hall thruster lifetime must take into account the >2 km/s, 3D ion drifts generated by the presence of magnetized waves in the cathode plume, as well as the various mechanisms for localized ion heating in different regions of the plasma.

Acknowledgments

This work was supported by a NASA Space Technology Graduate Research Opportunity. The authors would like to thank Vernon Chaplin for helpful discussion.

References

- [1] Boeuf, J.-P., "Tutorial: Physics and modeling of Hall thrusters," *Journal of Applied Physics*, Vol. 121, No. 1, 2017, p. 011101. <https://doi.org/10.1063/1.4972269>, URL <http://aip.scitation.org/doi/10.1063/1.4972269>.
- [2] Goebel, D. M., and Katz, I., *Fundamentals of Electric Propulsion*, John Wiley & Sons, Inc., Hoboken, NJ, USA, 2008. <https://doi.org/10.1002/9780470436448>, URL <http://doi.wiley.com/10.1002/9780470436448>.
- [3] Herman, D. A., Tofil, T. A., Santiago, W., Kamhawi, H., Polk, J. E., Snyder, J. S., Hofer, R. R., Picha, F. Q., Jackson, J., and Allen, M., "Overview of the Development and Mission Application of the Advanced Electric Propulsion System (AEPS)," *35th International Electric Propulsion Conference*, Atlanta, Georgia, 2017.
- [4] Fiehler, D., and Oleson, S., "A Comparison of Electric Propulsion Systems for Mars Exploration," *39th AIAA/ASME/SAE/ASEE Joint Propulsion Conference and Exhibit*, American Institute of Aeronautics and Astronautics, Reston, Virginia, 2003, pp. 1–7. <https://doi.org/10.2514/6.2003-4574>, URL <https://arc.aiaa.org/doi/10.2514/6.2003-4574>.
- [5] Hofer, R. R., Lobbia, R., Chaplin, V., Lopez Ortega, A., Mikellides, I., Polk, J., Kamhawi, H., Frieman, J., Huang, W., Peterson, P., and Herman, D., "Completing the Development of the 12.5 kW Hall Effect Rocket with Magnetic Shielding (HERMeS)," *36th International Electric Propulsion Conference*, Vienna, Austria, 2019.
- [6] Mikellides, I. G., Katz, I., Hofer, R. R., and Goebel, D. M., "Magnetic shielding of a laboratory Hall thruster. I. Theory and validation," *Journal of Applied Physics*, Vol. 115, No. 4, 2014, p. 043303. <https://doi.org/10.1063/1.4862313>, URL <http://aip.scitation.org/doi/10.1063/1.4862313>.
- [7] Hofer, R. R., Goebel, D. M., Mikellides, I. G., and Katz, I., "Magnetic shielding of a laboratory Hall thruster. II. Experiments," *Journal of Applied Physics*, Vol. 115, No. 4, 2014, p. 043304. <https://doi.org/10.1063/1.4862314>, URL <http://aip.scitation.org/doi/10.1063/1.4862314>.
- [8] Lopez Ortega, A., Mikellides, I. G., Sekerak, M. J., and Jorns, B. A., "Plasma simulations in 2-D (r-z) geometry for the assessment of pole erosion in a magnetically shielded Hall thruster," *Journal of Applied Physics*, Vol. 125, No. 3, 2019, p. 033302. <https://doi.org/10.1063/1.5077097>, URL <http://dx.doi.org/10.1063/1.5077097>.
- [9] Mikellides, I. G., Lopez Ortega, A., and Jorns, B., "Assessment of Pole Erosion in a Magnetically Shielded Hall Thruster," *50th AIAA/ASME/SAE/ASEE Joint Propulsion Conference*, American Institute of Aeronautics and Astronautics, Reston, Virginia, 2014, pp. AIAA–2014–3897. <https://doi.org/10.2514/6.2014-3897>, URL <http://arc.aiaa.org/doi/10.2514/6.2014-3897>.
- [10] Frieman, J. D., Gilland, J. H., Kamhawi, H., Mackey, J., Williams, G. J., Hofer, R. R., and Peterson, P. Y., "Wear trends of the 12.5 kW HERMeS Hall thruster," *Journal of Applied Physics*, Vol. 130, No. 14, 2021, p. 143303. <https://doi.org/10.1063/5.0062579>, URL <https://doi.org/10.1063/5.0062579><https://aip.scitation.org/doi/10.1063/5.0062579>.
- [11] Polk, J. E., Lobbia, R. B., Barriault, A., Guerrero, P., Mikellides, I. G., and Lopez Ortega, A., "Inner Front Pole Cover Erosion in the 12.5 kW HERMeS Hall Thruster Over a Range of Operating Conditions," *35th International Electric Propulsion Conference*, Electric Rocket Propulsion Society, Atlanta, Georgia, 2017, pp. IEPC–2017–409. URL http://erps.spacegrant.org/IEPC_2017/IEPC_2017_409.pdf%0Ahttps://iepc2017.org/sites/default/files/speaker-papers/iepc2017sla_measurements_final_0.pdf.
- [12] Lopez Ortega, A., Mikellides, I. G., Chaplin, V. H., Huang, W., and Frieman, J. D., "Anomalous Ion Heating and Pole Erosion in the 12.5-kW Hall Effect Rocket with Magnetic Shielding (HERMeS)," *AIAA Propulsion and Energy 2020 Forum*, American Institute of Aeronautics and Astronautics, Reston, Virginia, 2020, pp. AIAA 2020–3620. <https://doi.org/10.2514/6.2020-3620>, URL <https://arc.aiaa.org/doi/10.2514/6.2020-3620>.
- [13] Mikellides, I. G., and Lopez Ortega, A., "Cross-field Streaming Instabilities in the Lower Hybrid Frequency Near the Inner Pole Region of a Hall Thruster," 2020, pp. 1–13. <https://doi.org/10.2514/6.2020-3619>.

- [14] Jorns, B. A., Dodson, C., Anderson, J., Goebel, D. M., Hofer, R. R., Sekerak, M., Lopez Ortega, A., and Mikellides, I., "Mechanisms for Pole Piece Erosion in a 6-kW Magnetically-Shielded Hall Thruster," *Propulsion and Energy Forum*, 52nd AIAA/SAE/ASEE Joint Propulsion Conference, Salt Lake City, Utah, 2016, pp. AIAA 2016–4839. <https://doi.org/10.2514/6.2016-4839>.
- [15] Huang, W., and Kamhawi, H., "Counterstreaming ions at the inner pole of a magnetically shielded Hall thruster," *Journal of Applied Physics*, Vol. 129, No. 04, 2021, p. 043305. <https://doi.org/10.1063/5.0029428>, URL <https://doi.org/10.1063/5.0029428>.
- [16] Mikellides, I. G., and Lopez Ortega, A., "Growth of the lower hybrid drift instability in the plume of a magnetically shielded Hall thruster," *Journal of Applied Physics*, Vol. 129, No. 19, 2021, p. 193301. <https://doi.org/10.1063/5.0048706>, URL <https://aip.scitation.org/doi/10.1063/5.0048706>.
- [17] Jorns, B. A., and Hofer, R. R., "Plasma oscillations in a 6-kW magnetically shielded Hall thruster," *Physics of Plasmas*, Vol. 21, No. 5, 2014, p. 053512. <https://doi.org/10.1063/1.4879819>, URL <http://dx.doi.org/10.1063/1.4879819><http://aip.scitation.org/doi/10.1063/1.4879819>.
- [18] Jorns, B. A., Cusson, S. E., Brown, Z., and Dale, E., "Non-classical electron transport in the cathode plume of a Hall effect thruster," *Physics of Plasmas*, Vol. 27, No. 2, 2020, p. 022311. <https://doi.org/10.1063/1.5130680>, URL <http://aip.scitation.org/doi/10.1063/1.5130680>.
- [19] Hepner, S. T., Tang, E., Dale, E. T., and Jorns, B. A., "Rotational Waves in the Plume of an Externally-Mounted Hall Thruster Cathode," *AIAA Journal*, 2021, pp. 1–5. <https://doi.org/10.2514/1.J060578>, URL <https://arc.aiaa.org/doi/10.2514/1.J060578>.
- [20] Roberts, P. J., and Jorns, B. A., "Azimuthal Ion Drift in the Plume of a 9-kW Magnetically-Shielded Hall Thruster (Presentation Only)," *AIAA Propulsion and Energy 2021 Forum*, Virtual, ????
- [21] Roberts, P. J., Jorns, B. A., and Chaplin, V. H., "Experimental Characterization of Wave-Induced Azimuthal Ion Velocities in a Hollow Cathode Plume," *AIAA SciTech Forum*, San Diego, California, 2022, pp. AIAA 2022–1561. <https://doi.org/10.2514/6.2022-1561>.
- [22] Huang, W., Kamhawi, H., and Haag, T., "Plasma Oscillation Characterization of NASA's HERMeS Hall Thruster via High Speed Imaging," *52nd AIAA/SAE/ASEE Joint Propulsion Conference*, American Institute of Aeronautics and Astronautics, Reston, Virginia, 2016, pp. AIAA–2016–4829. <https://doi.org/10.2514/6.2016-4829>, URL <http://arc.aiaa.org/doi/10.2514/6.2016-4829>.
- [23] Brown, N. P., and Walker, M. L. R., "Review of Plasma-Induced Hall Thruster Erosion," *Applied Sciences*, Vol. 10, No. 11, 2020, p. 3775. <https://doi.org/10.3390/app10113775>, URL <https://www.mdpi.com/2076-3417/10/11/3775>.
- [24] Eckstein, W., and Preuss, R., "New fit formulae for the sputtering yield," *Journal of Nuclear Materials*, Vol. 320, No. 3, 2003, pp. 209–213. [https://doi.org/10.1016/S0022-3115\(03\)00192-2](https://doi.org/10.1016/S0022-3115(03)00192-2), URL <https://linkinghub.elsevier.com/retrieve/pii/S0022311503001922>.
- [25] Yim, J. T., "A Survey of Xenon Ion Sputter Yield Data and Fits Relevant to Electric Propulsion Spacecraft Integration," *35th International Electric Propulsion Conference*, Atlanta, Georgia, 2017, pp. IEPC–2017–060. URL <https://ntrs.nasa.gov/search.jsp?R=20170009068>.
- [26] Wei, Q., Li, K.-D., Lian, J., and Wang, L., "Angular dependence of sputtering yield of amorphous and polycrystalline materials," *Journal of Physics D: Applied Physics*, Vol. 41, No. 17, 2008, p. 172002. <https://doi.org/10.1088/0022-3727/41/17/172002>, URL <https://iopscience.iop.org/article/10.1088/0022-3727/41/17/172002>.
- [27] Meyer, M., Byrne, M., Jorns, B., and Boyd, I. D., "Erosion of a meshed reflector in the plume of a Hall effect thruster, Part 1: Modeling," *AIAA Propulsion and Energy 2019 Forum*, American Institute of Aeronautics and Astronautics, Reston, Virginia, 2019, pp. AIAA 2019–3987. <https://doi.org/10.2514/6.2019-3987>, URL <https://arc.aiaa.org/doi/10.2514/6.2019-3987>.
- [28] Byrne, M., Meyer, M., Boyd, I. D., and Jorns, B., "Erosion of Meshed Reflector in the Plume of a Hall Effect Thruster, Part 2: Experiments," *AIAA Propulsion and Energy 2019 Forum*, American Institute of Aeronautics and Astronautics, Reston, Virginia, 2019, pp. AIAA 2019–3988. <https://doi.org/10.2514/6.2019-3988>, URL <https://arc.aiaa.org/doi/10.2514/6.2019-3988>.
- [29] Hofer, R. R., Cusson, S. E., Lobbia, R. B., and Gallimore, A. D., "The H9 Magnetically Shielded Hall Thruster," *35th International Electric Propulsion Conference*, Atlanta, Georgia, 2017, pp. IEPC–2017–232. URL https://iepc2017.org/sites/default/files/speaker-papers/iepc-2017-232_hofer_r05.pdf.
- [30] Cusson, S. E., Hofer, R. R., Lobbia, R. B., Jorns, B. A., and Gallimore, A. D., "Performance of the H9 Magnetically Shielded Hall Thrusters," *35th International Electric Propulsion Conference*, Atlanta, Georgia, 2017, pp. IEPC–2017–239. URL https://iepc2017.org/sites/default/files/speaker-papers/iepc-2017-232_hofer_r05.pdf.

- [31] Viges, E. A., Jorns, B. A., Gallimore, A. D., and Sheehan, J. P., “University of Michigan’s Upgraded Large Vacuum Test Facility,” *36th International Electric Propulsion Conference*, Vienna, Austria, 2019, pp. 1–18.
- [32] Hansen, J. E., and Persson, W., “Revised analysis of singly ionized xenon, Xe II,” *Physica Scripta*, Vol. 36, No. 4, 1987, pp. 602–643. <https://doi.org/10.1088/0031-8949/36/4/005>, URL <https://iopscience.iop.org/article/10.1088/0031-8949/36/4/005>.
- [33] Durot, C. J., “Development of a Time-Resolved Laser-Induced Fluorescence Technique for Nonperiodic Oscillations,” Ph.D. thesis, University of Michigan, 2016.
- [34] Chaplin, V. H., Lobbia, R. B., Lopez Ortega, A., Mikellides, I. G., Hofer, R. R., Polk, J. E., and Friss, A. J., “Time-resolved ion velocity measurements in a high-power Hall thruster using laser-induced fluorescence with transfer function averaging,” *Applied Physics Letters*, Vol. 116, No. 23, 2020, p. 234107. <https://doi.org/10.1063/5.0007161>, URL <http://aip.scitation.org/doi/10.1063/5.0007161>.